Article type: Communication

Hexagonal PtBi Intermetallic Inlaid with Sub-Monolayer Pb Oxyhydroxide Boosts Methanol Oxidation

Wen Chen[#], Shuiping Luo[#], Mingzi Sun, Min Tang, Xiaokun Fan, Yu Cheng, Xiaoyu Wu, Yujia Liao, Bolong Huang and Zewei Quan**

Dr. W. Chen
School of Chemistry and Chemical Engineering, Harbin Institute of Technology, Harbin 15001, China

Dr. W. Chen, Dr. S. Luo, Dr. M. Tang, Dr. X. Fan, Dr. Y. Cheng, Dr. X. Wu, Y. Liao, Prof. Z. Quan
Department of Chemistry, Academy for Advanced Interdisciplinary Studies, and Guangdong Provincial Key Laboratory of Energy Materials for Electric Power, Southern University of Science and Technology (SUSTech), Shenzhen, Guangdong 518055, China
*E-mail: quanzw@sustech.edu.cn

Dr. W. Chen, Dr. S. Luo, Dr. M. Tang, Dr. X. Fan, Dr. Y. Cheng, Dr. X. Wu, Y. Liao, Prof. Z. Quan
Key Laboratory of Energy Conversion and Storage Technologies (Southern University of Science and Technology), Ministry of Education, Shenzhen 518055, China

M. Sun, Prof. B. Huang
Department of Applied Biology and Chemical Technology, The Hong Kong Polytechnic University, Hung Hom, Kowloon, Hong Kong SAR, China
*E-mail: bhuang@polyu.edu.hk

Keywords: intermetallic; Pb oxyhydroxide; methanol oxidation; electrocatalysis.

Abstract: Engineering multi-component nanocatalysts is effective to boost electrocatalysis in many applications, yet it remains a challenge in constructing well-defined multimetallic active sites at the atomic level. Herein, we report the surface inlay of sub-monolayer Pb oxyhydroxide onto hexagonal PtBi intermetallic nanoplates with intrinsically isolated Pt atoms, to boost the methanol oxidation reaction (MOR). The well-defined PtBi@6.4%Pb nanocatalyst exhibits 4.0/7.4 times higher mass activity than PtBi nanoplate/commercial Pt/C catalyst towards MOR in the alkaline electrolyte at 30 °C, and achieves a record-high mass activity of 51.07 A mg^{-1}_{Pt} at 60 °C, at which DMFCs would operate. DFT calculations reveal that the introduction of Pb oxyhydroxide on the surface not only promotes the electron transfer efficiency but also suppresses the CO poisoning effect, and the efficient p-d coupling

optimizes the electroactivity of PtBi@6.4%Pb nanoplates towards the MOR process with low reaction barriers.

Direct methanol fuel cells (DMFCs) have attracted widespread attention as promising power sources for portable devices because of their high energy density, environmental sustainability, and fuel safety. In the anode, methanol oxidation reaction (MOR) is a kinetically sluggish process with several orders of magnitude slower than hydrogen oxidation, seriously hindering the wide applications of DMFCs.[1-7] For complex MOR involving the transfer of multiple electrons, conventional Pt catalysts exhibit limited and quickly vanished catalytic activity arising from the severe poisoning of surface intermediates, especially CO. To develop practical Pt-based MOR electrocatalysts, composition engineering is an alternative strategy, which could enhance the adsorption of methanol, alleviate the adsorption of poisonous CO, and optimize the MOR process with low reaction barriers.[4, 8-11] In particular, isolating Pt atoms by forming intermetallic compounds is fascinating in terms of their long-range ordered nature and stable compositions.[12-20] In this respect, PtBi intermetallic nanocrystals exhibit high tolerance to poisonous CO, yet are accompanied by limited methanol adsorption and oxidation.[17, 21-24] On the other hand, surface modification of Pt nanocrystals via adatoms, deposited atoms, or doped atoms could significantly improve the electrocatalytic properties due to the geometric and electronic effects, but unfortunately, the active sites involved are usually distributed randomly.[25-36] Engineering multi-component nanocatalyst by combining the isolation and surface modification of Pt atoms via certain metals is expected to produce highly efficient Pt-based electrocatalysts towards MOR.

Herein, we construct hexagonal PtBi intermetallic nanoplates and then deposit trace Pb atoms on their ordered surface via a facile wet-chemistry method. The surface inlay of sub-monolayer Pb oxyhydroxide on PtBi substrate is achieved for the first time. The as-prepared PtBi@6.4%Pb nanoplates exhibit an ultra-high mass activity of 13.93 A mg^{-1}_{Pt} at around -0.2

V vs. SCE. Notably, such nanoplates achieve a record-high mass activity of 51.07 A mg^{-1}_{Pt} and excellent durability at 60 °C, at which DMFCs would operate. The *in situ* FTIR spectra show that the PtBi@6.4%Pb nanocatalyst possesses a superior ability in the oxidation of methanol and $HCOO^-$ intermediate, as well as in the quick release of adsorbed CO_2 to form CO_3^{2-}/HCO_3^-. DFT calculations unravel that the robust valence states of Pt sites are due to the p-d coupling of Bi and Pb sites, which facilitates the fast site-to-site electron transfer from nanoplate surface to intermediates. The optimized electronic structures further lead to the low energy barriers in the MOR process.

The PtBi@6.4%Pb nanoplates are synthesized by decomposing $Pb(acac)_2$ at 260 °C in the reaction solution containing as-formed PtBi intermetallic nanoplates (**Figure S1, the Supporting Information**), and the experimental details are shown in the Supporting Information. The high-angle annular dark-field scanning transmission electron microscopy (HAADF-STEM) and transmission electron microscopy (TEM) images in **1a** and **b** show that the products are well-dispersed hexagonal nanoplates, of which the average edge length is about 6.8 nm (**Figure S2**). The atomic ratio of Pt/Bi/Pb in this sample is determined to be 46.9/46.7/6.4 via the energy-dispersive X-ray spectroscopy (EDX) result (**Figure S3**), which is in good agreement with the ratio (Pt//Bi/Pb= 46.6/46.7/6.7) from the inductively coupled plasma mass spectrometry (ICP-MS). According to the XRD pattern in **Figure 1c,** the diffraction peaks are consistent with that of standard PtBi intermetallic (ICSD #58845), revealing the dominant hexagonal close packed (*hcp*) structure of these PtBi@6.4%Pb nanoplates, and the low loading of Pb species on the surface.

The atomic arrangement in the PtBi@6.4%Pb nanoplates is uncovered by the aberration-corrected HAADF-STEM characterizations. As shown in **Figures 1d-f,** the *hcp* structure is clearly demonstrated by the rhomboid periodic patterns viewed along the [001] zone axis. The lattice spacing of the crystal planes parallel to the edge is measured to be 0.378 nm, corresponding to the (100) planes in *hcp* PtBi intermetallic. As shown in **Figure 1g**, the

integrated pixel intensities along the red dashed line marked in **Figure 1f** exhibit a periodic arrangement of two weak peaks between two strong peaks, consistent with the atomic arrangement of PtBi intermetallic. In the HAADF-STEM image of the PtBi@6.4%Pb nanoplate (**Figure 1f**), the bright dots can be attributed to the Pt atomic columns and dark dots to the Bi atomic columns. This brightness difference partially originates from the existence of three Pt atoms and only one Bi atom in their atomic columns inside a unit cell along the [001] zone axis, respectively. **Figure S4** shows the periodic intensities across the whole hexagonal nanoplate, which also match well with the atomic arrangement in PtBi intermetallic. In addition, the EDX mapping results in **Figure 1h** show the uniform distribution of Pt, Bi, and Pb elements over the hexagonal nanoplate. [13, 37-39]

The distribution of deposited Pb atoms on the nanoplate surface is further analyzed in detail. In the enlarged HAADF-STEM image of a typical edge in **Figure 2a,** some dark dots within a sub-monolayer (marked by the red dashed cycles) are observed on the outermost surface of PtBi@6.4%Pb nanoplates. **Figure 2b** displays the corresponding atomic arrangement of Pt/Bi/Pb atoms in this HAADF-STEM image, based on the detailed analyses on the intensity profiles of these different sites on the surface (**Figure 2c**, **Figure S5**, and **Figure S6**). For example, the intensity profiles of L1 and L3 illustrate two typical arrangements of Pt-Bi-Bi and Bi-Pt-Bi atoms on nanoplate surface, respectively. In comparison, the intensity profiles of L2 (vs. L1) and L4 (vs. L3) that contain red dashed cycles exhibit additional weak peaks on the top of Pt-Bi-Bi and Bi-Pt-Bi atoms with varied interatomic distances, respectively. According to the XPS in-depth analyses of these PtBi@6.4%Pb nanoplates shown in **Figure 2d**, the intensity of Pb^{2+} $4f_{7/2}$ peak decreases rapidly with the increase of sputtering time, while the intensities of Bi^{3+} $4f_{7/2}$ and Pt^{0} $4f_{7/2}$ peaks remain unchanged. These results reveal Pb atoms are located on the PtBi nanoplate surface, as illustrated in **Figure 2f**.

In addition, as indicated by the XPS results in **Figures 2e** and **S7**, Pt atoms are mainly in zero valence state (65%) and Bi atoms are mainly in oxidation state (86%), while Pb atoms

are in the full oxidation state (PbO). Compared with Pt/C, the binging energy of Pt 4f peaks in the PtBi intermetallic nanoplates shift to lower binding energy by 0.22 eV (**Figure S7**). In the PtBi@6.4%Pb nanoplates, these Pt 4f peaks further shift to a lower binding energy while the Bi 4f peaks shift to higher binding energy, compared with the PtBi intermetallic nanoplates (**Figures 2e** and **S7**). These results underline the electrons transfer from Bi to Pt.[37-42] To figure out the variations of surface Bi and Pb species during the MOR polarization process, PtBi@6.4%Pb nanoplates were loaded on carbon cloth for the same electrochemical activation in Ar-saturated 1 M KOH + 1 M CH_3OH solution. As shown in **Figure S8**, the peaks at 532.70 eV, 531.58 eV, and 530.42 eV of the adsorbed O 1s can be assigned to H_2O, metal-OH (M-OH), and metal-O (M-O) species, respectively.[43] There is a noticeable increase in the M-OH peak intensity after electrochemical activation, along with an increase in the integrated area ratio of M-OH/M-O from 0.29 to 0.80. At the same time, the intensity of metallic Bi peak is greatly decreased as the integrated area ratio of Bi^0/Bi^{3+} decreases from 0.42 to 0.20. Moreover, the negative shift of Pb^{2+} 4f peaks by 0.13 eV is observed after electrochemical activation. As the binding energy of Pb-OH peak (138.4 eV) is lower than that of Pb-O (138.9 eV), this shift indicates the formation of $PbO_x(OH)_y$ in the KOH electrolyte, which is also supported by the increased M-OH peak intensity in the O 1s spectra. These characterizations demonstrate that Bi oxyhydroxide ($BiO_x(OH)_y$) and Pb oxyhydroxide ($PbO_x(OH)_y$) are in-situ formed on the nanoplate surface during MOR electrocatalysis.[44-46]

The MOR activities of PtBi, PtBi@3.1%Pb, PtBi@6.4%Pb, and PtBi@9.3%Pb nanoplates in alkaline electrolyte are systemically evaluated after they are loaded with the commercial carbon and washed by a hexane/ethanol/1-butylamine mixture (**Figures S9** and **S10**). **Figures 3a** and **S11a** show the cyclic voltammograms (CVs) of these electrocatalysts recorded in Ar-saturated 1 M KOH solution. Compared with Pt/C, the hydrogen adsorption/desorption peaks (-1.0 V to -0.6 V vs. SCE) of the PtBi and PtBi@Pb catalysts are obviously suppressed, due to the exposure of Bi/Pb species and the formation of isolated Pt sites. As shown by the positive-

going MOR polarization curves recorded in Ar-saturated 1 M KOH + 1 M CH_3OH solution at 30 °C (**Figures 3b** and **S11b**), the PtBi intermetallic nanoplates display a higher peak mass activity than Pt/C. Notably, the PtBi@6.4%Pb nanoplates exhibit the highest peak mass activity of 13.93 A mg^{-1}_{Pt}, which is 4.0 and 7.4 times higher than those of PtBi nanoplates and Pt/C, respectively, outperforming most of the advanced MOR electrocatalysts (**Figure 3e**).[47-52] As known, DMFCs typically operate at around 60 °C due to internal heating. To evaluate the practical electrocatalytic performances of these PtBi@6.4%Pb nanoplates, MOR tests of PtBi@6.4%Pb nanoplates at different temperatures (45 °C and 60 °C) are performed, using commercial Pt/C as the benchmark.[32] **Figures 3c** and **d** show that the electrocatalytic activities of the catalysts are significantly enhanced towards MOR at higher temperatures, which could originate from the promotion of reaction kinetics and/or alleviation of CO poisoning at elevated temperatures.[32, 53-54] Especially, the PtBi@6.4%Pb nanoplates exhibit a record-high mass activity of 51.07 A mg^{-1}_{Pt} at 60 °C (**Figure 3e**), which is 3.2 times higher than that of Pt/C under the same conditions. As shown by the chronoamperometry (CA) curves measured at -0.3 V vs. SCE at 60 °C (**Figure 3f**), the current density of PtBi@6.4%Pb nanoplates after 20,000 s retains 60.9% of the initial value, which is much higher than that of Pt/C (29.4%) and indicates the excellent durability of PtBi@6.4%Pb nanoplates. In addition, the superior tolerances to CO poisoning on these PtBi intermetallic nanoplates-based catalysts are revealed by the CO-stripping experiments. As shown in **Figures 3g** and **S12**, the oxidation peaks (-0.36 V vs. SCE) of absorbed CO are significantly suppressed on these PtBi@Pb and PtBi nanoplates, compared with Pt/C. The results can be attributed to the isolation of Pt atoms and the exposure of Bi/Pb species on these intermetallic compounds. [13, 23]

Figures 3h and **S13** show the *in situ* FTIR spectra of PtBi@6.4%Pb nanoplates, PtBi nanoplates and Pt/C catalyst towards MOR in alkaline electrolyte. There are four main vibration bands, namely the vibration band of CO_2 (~ 2345 cm^{-1}), the asymmetric stretching vibration band of $HCOO^-$ (~ 1585 cm^{-1}), the symmetric vibration twin bands of $HCOO^-$ (~

1381 cm^{-1} and 1348 cm^{-1}), and the wide vibration band of CO_3^{2-}/HCO_3^- (~ 1376 cm^{-1}).[17, 32, 55-56] As for the PtBi@6.4%Pb nanoplates (**Figure 3h**), the $HCOO^-$ peak appears at a potential as low as -0.7 V vs. SCE that is obviously lower than those of PtBi (-0.5 V) and Pt/C (-0.5 V). The CO_2 and CO_3^{2-}/HCO_3^- vibration peaks appear as the potential increases to -0.3 V that is lower than that of PtBi (-0.1 V). Such results indicate that PtBi@6.4%Pb nanoplates exhibit an enhanced ability to oxidize methanol and $HCOO^-$ intermediate into CO_2 at lower potentials. Subsequently, the peak intensity of $HCOO^-$ gradually decreases and the peak intensities of both CO_2 and CO_3^{2-}/HCO_3^- gradually increase. The peak intensity of CO_2 rapidly decreases while that of CO_3^{2-}/HCO_3^- increases as the potential increases to -0.1 V, which is also lower than that of PtBi (0 V). These results indicate the desorption of adsorbed CO_2 to form CO_3^{2-}/HCO_3^-. Thus, these features endow PtBi@6.4%Pb nanoplates with superior MOR electrocatalytic performances, compared to Pt/C and PtBi nanoplates.[32, 57-59]

Theoretical calculations based on DFT are further introduced to explore the mechanism of improved MOR performances on PtBi@6.4%Pb. The relaxed lattice structure and electronic distributions of bonding and anti-bonding orbitals near the Fermi level (E_F) on PtBi@6.4%Pb are demonstrated in **Figures 4a** and **b.** The surface introduction of Pb oxyhydroxide has not caused any evident distortions to the lattice structure. Meanwhile, the *OH and *O species on the surface show the evident contribution to the bonding orbitals while the Pb sites dominate the anti-bonding orbitals. The more electroactive surface of PtBi@6.4%Pb determines the higher electroactivity for the MOR process than PtBi. The detailed electronic structures of PtBi@6.4%Pb are demonstrated through the projected partial density of states (PDOS) (**Figure 4c**). Notably, the Pt-5d orbitals display an evident peak at E_V-2.68 eV (E_V = 0 eV) and the high d-band center at E_V-2.49 eV demonstrates the high electroactivity for the MOR process. It is noted that O-s, p orbitals show a good overlapping with Pb orbitals, supporting the strong binding and efficient site-to-site electron transfer of the electrocatalyst. Pb-6p orbitals exhibit broad coverage crossing the E_F with the main contribution at the anti-bonding

orbitals, which facilitates the binding of intermediates on the surface. Meanwhile, the high electron density of Bi-s, p orbitals near E_F further contributes to the electron transfer between the electrocatalyst surface and the adsorbed intermediates. The electronic structure of PtBi@6.4%Pb has confirmed that the introduction of Pb oxyhydroxide optimizes surface electroactivity. Then, the site-to-site electronic structures of the electrocatalyst are further compared regarding Pt-5d, Bi-6p, and O-s, p orbitals (**Figure 4d**). From the bulk of electrocatalyst to the surface, Pt-5d orbitals show a gradual upshift, where the dominant peak shift from E_V-2.74 eV to E_V-2.02 eV with improved electroactivity. In particular, the introduction of Pb oxyhydroxide slightly suppresses the Pt-5d orbitals, which prevents the over-binding of CO to avoid the poisoning effect on the electrocatalyst. For the Bi-6p orbitals, the range enlarges obviously from the bulk to the surface, which protects the robust electronic structure of surface Pt sites (**Figure 4e**). The electron density is improved at the surface, which guarantees the high electron transfer efficiency within the PtBi. For the surface *O and *OH species, their electroactivity should also be considered (**Figure 4f**). As the coordination environment changes, the s, p orbitals upshift towards the E_F with improved electroactivity. Therefore, the electronic structure of the surface has revealed the robust electroactivity induced by the introduction of surface Pb oxyhydroxide.

Furthermore, we also investigate the MOR reaction trend from the energetic perspective. For the MOR process, the stable adsorption configurations of key adsorbates near the Pb sites are shown in **Figure S14**. As for the adsorption of CH_3OH, the surface Pb sites show even stronger binding strength than the Pt sites, which indicates the improved adsorption of reactants in promoting electrocatalysis (**Figure 4g**). Meanwhile, the CO_2 adsorption is favored on Pt and Pb sites while the adsorption of CO is unfavored on Pb sites. The distinct binding preferences indicate the introduction of surface Pb further suppresses CO poisoning during MOR. Then, the reaction pathway further confirms the stronger reaction trend of MOR (**Figure 4h**). For the initial dehydrogenation of CH_3OH, the reaction undergoes a continuous

downhill trend until the formation of *CHOH species. Further dehydrogenation determines the reaction selectivity towards CO. Notably, the CO reaction pathway meets an uphill reaction trend with two energy barriers of 0.36 and 0.50 eV, respectively. A further barrier of *COOH formation (0.46 eV) demonstrates that the CO reaction pathway for MOR is very challenging. In comparison, there is only one barrier for the CO_2 pathway with the conversion from *CHO to *HCOOH of 0.69 eV. The following reaction steps to generate CO_2 are exothermic with high efficiency. The overall MOR process is exothermic, releasing 0.75 eV energy. Therefore, the high electroactivity of PtBi@6.4%Pb towards MOR has been unraveled from both electronic structures and reaction energies.

In summary, we successfully construct the sub-monolayer Pb on the fully ordered PtBi nanoplates. The distribution of Pt/Bi/Pb atoms is clearly resolved at the atomic level and the Pb species is determined to be $PbO_x(OH)_y$ during MOR electrocatalysis. The well-defined PtBi@6.4%Pb nanocatalyst exhibits a record-high mass activity of 51.07 A mg^{-1}_{Pt} at 60 °C, excellent durability, and high tolerance to CO poisoning, representing a state-of-the-art electrocatalyst towards MOR in alkaline electrolyte. The *in situ* FTIR spectra illustrate the enhanced ability of PtBi@6.4%Pb nanoplates in oxidizing CH_3OH and the $HCOO^-$ intermediate, as well as in releasing adsorbed CO_2 quickly. DFT calculations demonstrate that the introduction of Pb oxyhydroxide on the surface optimizes the electronic structure of PtBi@6.4%Pb through efficient p-d coupling. Meanwhile, the Pb sites enable the suppression of CO over-binding and promote adsorption of CH_3OH and desorption of CO_2 to facilitate the MOR.

Experimental Section

Experimental details are provided in the Supporting Information.

Supporting Information

Supporting Information is available from the Wiley Online Library or from the author.

Acknowledgements

This work was supported by the National Natural Science Foundation of China (NSFC) (Grant 52101259 and 21771156), the Science and Technology Cooperation Fund between Chinese and Australian Governments (Grants 2017YFE0132300 and ACSRF65827), the Guangdong Science and Technology Department (Grants 2016ZT06C279 and 2016ZT06C279), and the Shenzhen Science and Technology Innovation Committee (Grant KQTD2016053019134356). The authors acknowledge the assistance of SUSTech Core Research Facilities.

Received: ((will be filled in by the editorial staff))
Revised: ((will be filled in by the editorial staff))
Published online: ((will be filled in by the editorial staff))

References

[1] Y. Wang, K. S. Chen, J. Mishler, S. C. Cho, X. C. Adroher, *Appl. Energy* **2011**, *88*, 981.

[2] M. Shao, Q. Chang, J. P. Dodelet, R. Chenitz, *Chem. Rev.* **2016**, *116*, 3594.

[3] X. Du, S. Luo, H. Du, M. Tang, X. Huang, P. K. Shen, *J. Mater. Chem. A* **2016**, *4*, 1579.

[4] J. Zhu, Y. Yang, L. Chen, W. Xiao, H. Liu, H. D. Abruña, D. Wang, *Chem. Mater.* **2018**, *30*, 5987.

[5] Y. Kang, J. B. Pyo, X. Ye, T. R. Gordon, C. B. Murray, *ACS Nano* **2012**, *6*, 5642.

[6] F. Zhao, L. Zheng, Q. Yuan, X. Yang, Q. Zhang, H. Xu, Y. Guo, S. Yang, Z. Zhou, L. Gu, X. Wang, *Adv. Mater.* **2021**, e2103383.

[7] T. Iwasita, *Electrochim. Acta* **2002**, *47*, 3663.

[8] H. L. Liu, F. Nosheen, X. Wang, *Chem. Soc. Rev.* **2015**, *44*, 3056.

[9] T. Ghosh, B. M. Leonard, Q. Zhou, F. J. DiSalvo, *Chem. Mater.* **2010**, *22*, 2190.

[10] S. Luo, M. Tang, P. K. Shen, S. Ye, *Adv. Mater.* **2017**, *29*, 1601687.

[11] X. Zhu, L. Huang, M. Wei, P. Tsiakaras, P. K. Shen, *Appl. Catal. B - Environ.* **2021**, *281*, 119460.

[12] J. Guo, L. Gao, X. Tan, Y. Yuan, J. Kim, Y. Wang, H. Wang, Y. J. Zeng, S. I. Choi, S. C. Smith, H. Huang, *Angew. Chem. Int. Ed.* **2021**, *60*, 10942.

[13] S. Luo, W. Chen, Y. Cheng, X. Song, Q. Wu, L. Li, X. Wu, T. Wu, M. Li, Q. Yang, K. Deng, Z. Quan, *Adv. Mater.* **2019**, *31*, 1903683.

[14] G. Zhang, C. Ye, W. Liu, X. Zhang, D. Su, X. Yang, J. Z. Chen, Z. Wu, J. T. Miller, *Nano Lett.* **2019**, *19*, 4380.

[15] X. Ji, K. T. Lee, R. Holden, L. Zhang, J. Zhang, G. A. Botton, M. Couillard, L. F. Nazar, *Nat. Chem.* **2010**, *2*, 286.

[16] D. Wang, H. L. Xin, R. Hovden, H. Wang, Y. Yu, D. A. Muller, F. J. DiSalvo, H. D. Abruña, *Nat. Mater.* **2013**, *12*, 81.

[17] Y. Qin, M. Luo, Y. Sun, C. Li, B. Huang, Y. Yang, Y. Li, L. Wang, S. Guo, *ACS Catal.* **2018**, *8*, 5581.

[18] Y. Yan, J. S. Du, K. D. Gilroy, D. Yang, Y. Xia, H. Zhang, *Adv. Mater.* **2017**, *29*, 1605997.

[19] Q. Feng, S. Zhao, D. He, S. Tian, L. Gu, X. Wen, C. Chen, Q. Peng, D. Wang, Y. Li, *J. Am. Chem. Soc.* **2018**, *140*, 2773.

[20] Q. Wang, Z. L. Zhao, Z. Zhang, T. Feng, R. Zhong, H. Xu, S. T. Pantelides, M. Gu, *Adv. Sci.* **2019**, *7*, 1901279.

[21] D. Zhang, F. Wu, M. Peng, X. Wang, D. Xia, G. Guo, *J. Am. Chem. Soc.* **2015**, *137*, 6263.

[22] M. A. Ud Din, F. Saleem, B. Ni, Y. Yong, X. Wang, *Adv. Mater.* **2017**, *29*, 1604994.

[23] Y. Feng, Q. Shao, F. Lv, L. Bu, J. Guo, S. Guo, X. Huang, *Adv. Sci.* **2020**, *7*, 1800178.

[24] X. Yuan, X. Jiang, M. Cao, L. Chen, K. Nie, Y. Zhang, Y. Xu, X. Sun, Y. Li, Q. Zhang, *Nano Res.* **2019**, *12*, 429.

[25] J. Lim, H. Shin, M. Kim, H. Lee, K. S. Lee, Y. Kwon, D. Song, S. Oh, H. Kim, E. Cho, *Nano Lett.* **2018**, *18*, 2450.

[26] X. Huang, Z. Zhao, L. Cao, Y. Chen, E. Zhu, Z. Lin, M. Li, A. Yan, A. Zettl, Y. M. Wang, X. Duan, T. Mueller, Y. Huang, *Science* **2015**, *348*, 1230.

[27] S. Luo, L. Zhang, Y. Liao, L. Li, Q. Yang, X. Wu, X. Wu, D. He, C. He, W. Chen, Q. Wu, M. Li, E. J. M. Hensen, Z. Quan, *Adv. Mater.* **2021**, *33*, e2008508.

[28] X. Yang, K. X. Yao, J. Y. Ye, Q. Yuan, F. Zhao, Y. Li, Z. Zhou, *Adv. Funct. Mater.* **2021**, *31*, 2103671.

[29] J. Liang, N. Li, Z. Zhao, L. Ma, X. Wang, S. Li, X. Liu, T. Wang, Y. Du, G. Lu, J. Han, Y. Huang, D. Su, Q. Li, *Angew. Chem. Int. Ed.* **2019**, *58*, 15471.

[30] M. Tang, W. Chen, S. Luo, X. Wu, X. Fan, Y. Liao, X. Song, Y. Cheng, L. Li, L. Tan, Y. Liu, Z. Quan, *J. Mater. Chem. A* **2021**, *9*, 9602.

[31] J. Zhang, M. Yuan, T. Zhao, W. Wang, H. Huang, K. Cui, Z. Liu, S. Li, Z. Li, G. Zhang, *J. Mater. Chem. A* **2021**, DOI: 10.1039/D1TA06015E.

[32] F. Zhao, J. Ye, Q. Yuan, X. Yang, Z. Zhou, *J. Mater. Chem. A* **2020**, *8*, 11564.

[33] M. Li, Z. Zhao, W. Zhang, M. Luo, L. Tao, Y. Sun, Z. Xia, Y. Chao, K. Yin, Q. Zhang, L. Gu, W. Yang, Y. Yu, G. Lu, S. Guo, *Adv. Mater.* **2021**, e2103762.

[34] P. N. Duchesne, Z. Y. Li, C. P. Deming, V. Fung, X. Zhao, J. Yuan, T. Regier, A. Aldalbahi, Z. Almarhoon, S. Chen, D. E. Jiang, N. Zheng, P. Zhang, *Nat. Mater.* **2018**, *17*, 1033.

[35] J. V. Perales-Rondón, A. Ferre-Vilaplana, J. M. Feliu, E. Herrero, *J. Am. Chem. Soc.* **2014**, *136*, 13110.

[36] A. Ferre-Vilaplana, J. V. c. Perales-Rondón, J. M. Feliu, E. Herrero, *ACS Catal.* **2014**, *5*, 645.

[37] L. Bu, N. Zhang, S. Guo, X. Zhang, J. Li, J. Yao, T. Wu, G. Lu, J. Y. Ma, D. Su, X. Huang, *Science* **2016**, *354*, 1410.

[38] B. E, Q. Shao, L. Bu, S. Bai, Y. Li, X. Huang, *Adv. Energy Mater.* **2018**, *8*, 1703430.

[39] Z. Zhu, F. Liu, J. Fan, Q. Li, Y. Min, Q. Xu, *ACS Appl. Mater. Interfaces* **2020**, *12*, 52731.

[40] L. Chen, L. Zhou, H. Lu, Y. Zhou, J. Huang, J. Wang, Y. Wang, X. Yuan, Y. Yao, *Chem. Commun.* **2020**. Ref not complete

[41] Q. Wang, G. J. Xia, Z. L. Zhao, Y. Zhu, X. Shi, L. Huang, Y. G. Wang, M. Gu, *Nano Energy* **2020**, *76*. Ref not complete

[42] Q. Wang, Z. L. Zhao, M. Gu, *Small* **2019**, *15*, 1903122.

[43] Y. Chen, W. Cai, C. Dang, J. Fan, J. Zhou, Z. Liu, *Chem. Eng. Res. Des.* **2020**, *161*, 332.

[44] X. Yuan, Y. Zhang, M. Cao, T. Zhou, X. Jiang, J. Chen, F. Lyu, Y. Xu, J. Luo, Q. Zhang, Y. Yin, *Nano Lett.* **2019**, *19*, 4752.

[45] X. Wang, M. Xie, F. Lyu, Y. M. Yiu, Z. Wang, J. Chen, L. Y. Chang, Y. Xia, Q. Zhong, M. Chu, H. Yang, T. Cheng, T. K. Sham, Q. Zhang, *Nano Lett.* **2020**, *20*, 7751.

[46] X. Yuan, B. Jiang, M. Cao, C. Zhang, X. Liu, Q. Zhang, F. Lyu, L. Gu, Q. Zhang, *Nano Res.* **2020**, *13*, 265.

[47] J. Huang, Y. Liu, M. Xu, C. Wan, H. Liu, M. Li, Z. Huang, X. Duan, X. Pan, Y. Huang, *Nano Lett.* **2019**, *19*, 5431.

[48] M. Li, K. Duanmu, C. Wan, T. Cheng, L. Zhang, S. Dai, W. Chen, Z. Zhao, P. Li, H. Fei, Y. Zhu, R. Yu, J. Luo, K. Zang, Z. Lin, M. Ding, J. Huang, H. Sun, J. Guo, X. Pan, W. A. Goddard, P. Sautet, Y. Huang, X. Duan, *Nat. Catal.* **2019**, *2*, 495.

[49] X. Wu, Y. Jiang, Y. Yan, X. Li, S. Luo, J. Huang, J. Li, R. Shen, D. Yang, H. Zhang, *Adv. Sci.* **2019**, *6*, 1902249.

[50] L. Chen, X. Liang, X. Li, J. Pei, H. Lin, D. Jia, W. Chen, D. Wang, Y. Li, *Nano Energy* **2020**, *73*, 104784.

[51] H. Li, Y. Han, H. Zhao, W. Qi, D. Zhang, Y. Yu, W. Cai, S. Li, J. Lai, B. Huang, L. Wang, *Nat. Commun.* **2020**, *11*, 5437.

[52] S. Zhang, Z. Zeng, Q. Li, B. Huang, X. Zhang, Y. Du, C. H. Yan, *Energ. Environ. Sci.* **2021**, DOI: 10.1039/D1EE02433G.

[53] A. Yuda, A. Ashok, A. Kumar, *Catal. Rev.* **2020**, DOI: 10.1080/01614940.2020.1802811.

[54] A. V. Tripković, K. D. Popović, B. N. Grgur, B. Blizanac, P. N. Ross, N. M. Marković, *Electrochim. Acta* **2002**, *47*, 3707.

[55] Z. Liang, L. Song, S. Deng, Y. Zhu, E. Stavitski, R. R. Adzic, J. Chen, J. X. Wang, *J. Am. Chem. Soc.* **2019**, *141*, 9629.

[56] J. X. Tang, Q. S. Chen, L. X. You, H. G. Liao, S. G. Sun, S. G. Zhou, Z. N. Xu, Y. M. Chen, G. C. Guo, *J. Mater. Chem. A* **2018**, *6*, 2327.

[57] B. W. Zhang, Y. X. Jiang, J. Ren, X. M. Qu, G. L. Xu, S. G. Sun, *Electrochim. Acta* **2015**, *162*, 254.

[58] J. Y. Ye, Y. X. Jiang, T. Sheng, S. G. Sun, *Nano Energy* **2016**, *29*, 414.

[59] F. Yang, J. Ye, Q. Yuan, X. Yang, Z. Xie, F. Zhao, Z. Zhou, L. Gu, X. Wang, *Adv. Funct. Mater.* **2020**, *30*, 1908235.

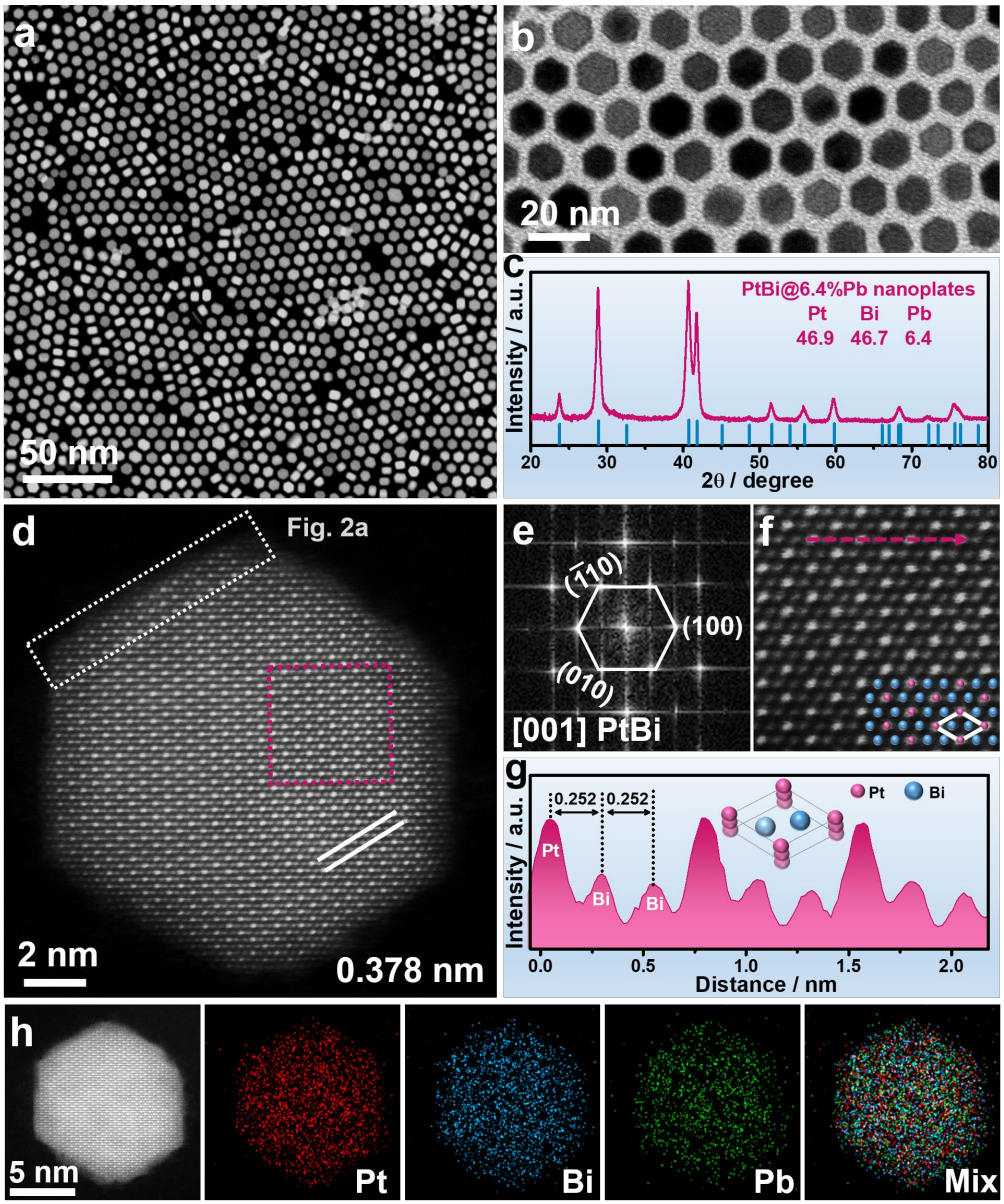

Figure 1. a) HAADF-STEM image, (b) TEM image, and (c) XRD pattern of the PtBi@6.4%Pb nanoplates. d) Aberration-corrected HAADF-STEM image of a typical PtBi@6.4%Pb nanoplate. e) Corresponding FFT pattern of Figure 1d viewed along *hcp* PtBi [001] zone axis. f) Enlarged HAADF-STEM image from the area indicated by the red dashed rectangle in Figure 1d. g) The line intensity profiles taken along the red dashed line in Figure 1f. The inset in (g) shows the unit cell of PtBi intermetallic. h) EDX mapping images of a PtBi@6.4%Pb nanoplate.

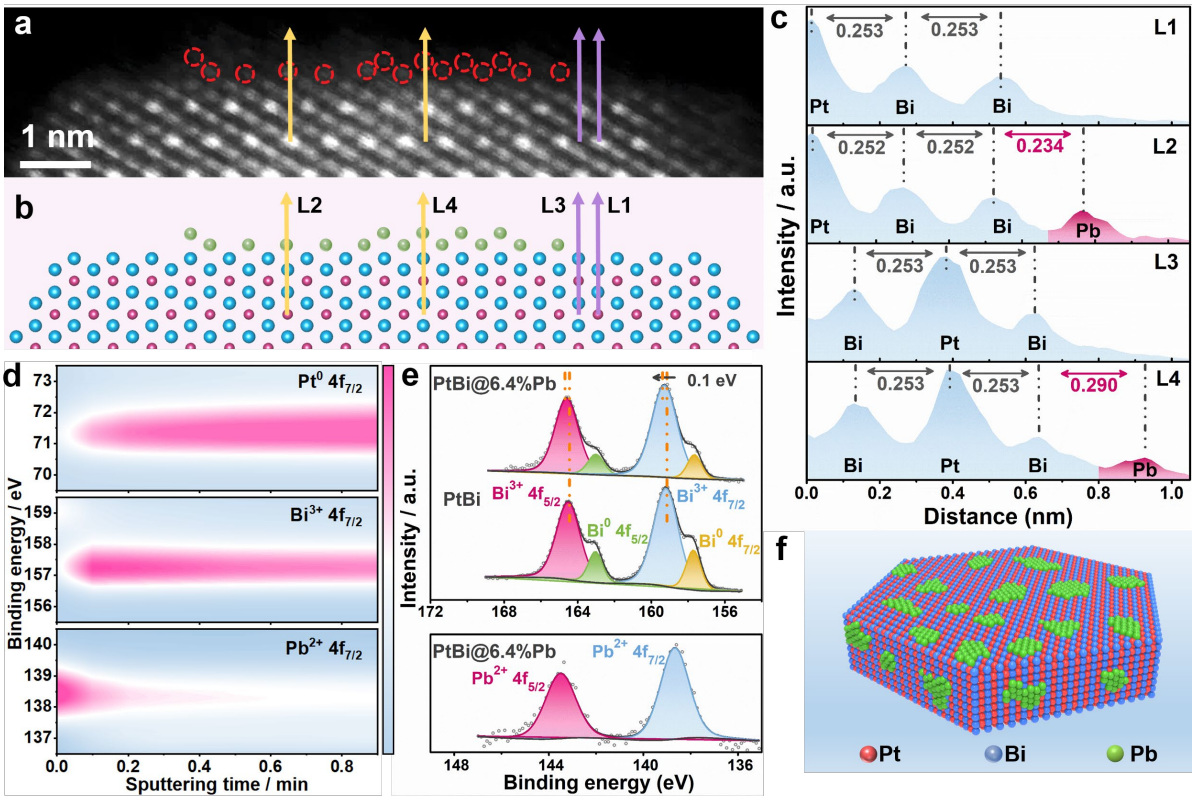

Figure 2. a) Typical HAADF-STEM image of the edge region as marked by the white dashed rectangle in Figure 1d. b) The corresponding atomic arrangement based on the HAADF-STEM image in Figure 1a. Red, blue, and green spheres represent Pt, Bi, and Pb atoms, respectively. c) The intensity profiles taken along the yellow and purple lines shown in Figure 2a. d) XPS in-depth analyses of the PtBi@6.4%Pb nanoplates with different sputtering time. e) Bi 4f and Pb 4f XPS spectra of the PtBi@6.4%Pb nanoplates and PtBi nanoplates. f) The schematic illustration showing the atomic arrangement of Pt/Bi/Pb atoms in the PtBi@6.4%Pb nanoplate.

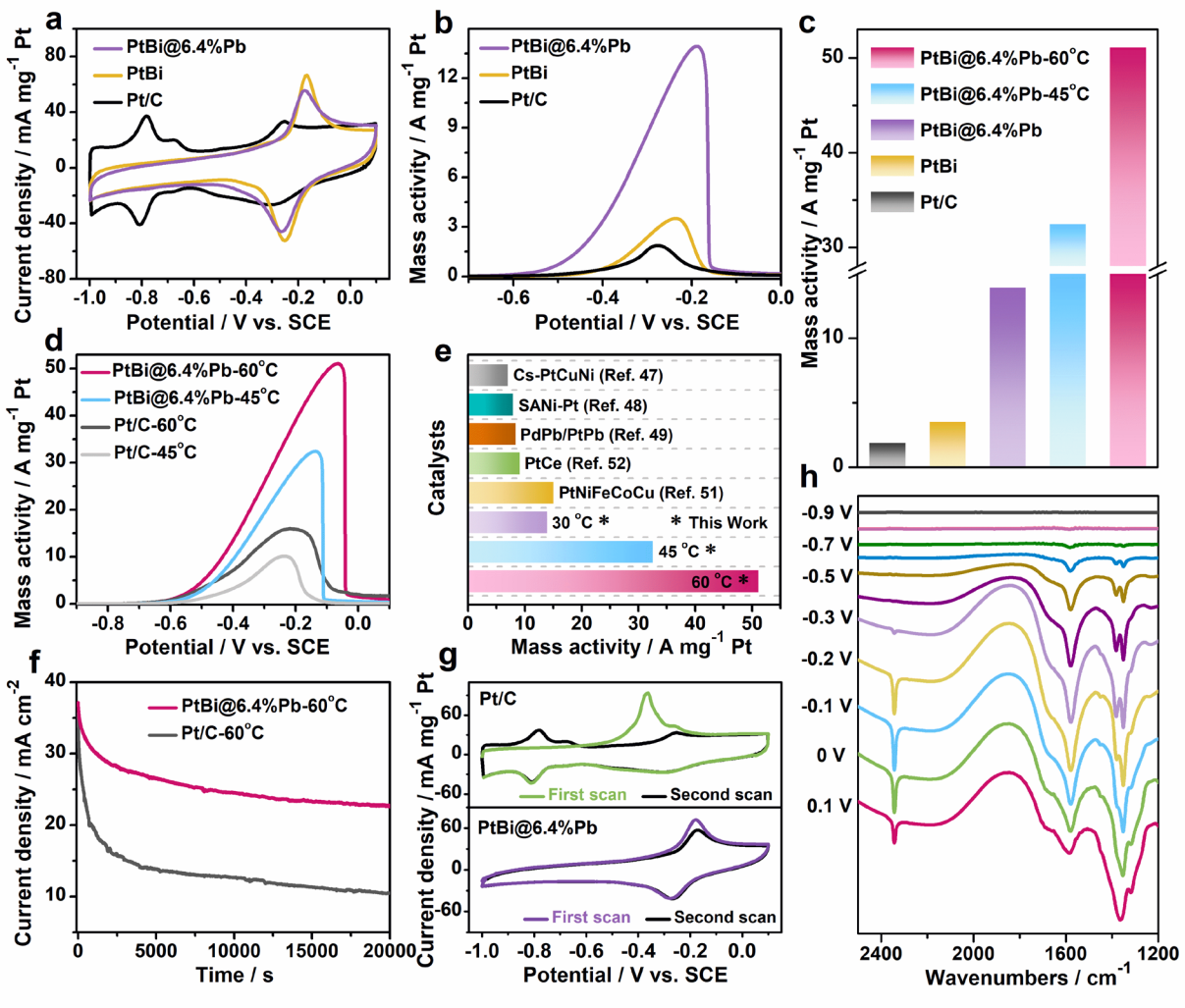

Figure 3. a) CV curves and (b) positive-going MOR polarization curves of different catalysts recorded at a scan rate of 50 mV s^{-1}. c) The histogram of mass activities of different catalysts. d) Positive-going MOR polarization curves of PtBi@6.4%Pb nanoplates and Pt/C catalysts recorded at different temperatures. e) The comparisons on the catalytic performance between PtBi@6.4%Pb nanoplates and other advanced MOR catalysts in alkaline electrolyte. f) Long-term chronoamperometry of PtBi@6.4%Pb nanoplates and Pt/C recorded at -0.3 V vs. SCE at 60 °C. g) CO-stripping curves of PtBi@6.4%Pb nanoplates and Pt/C catalysts. h) The in-situ FTIR spectra of PtBi@6.4%Pb nanoplates recorded in Ar-saturated 1 M KOH + 1 M CH_3OH solution.

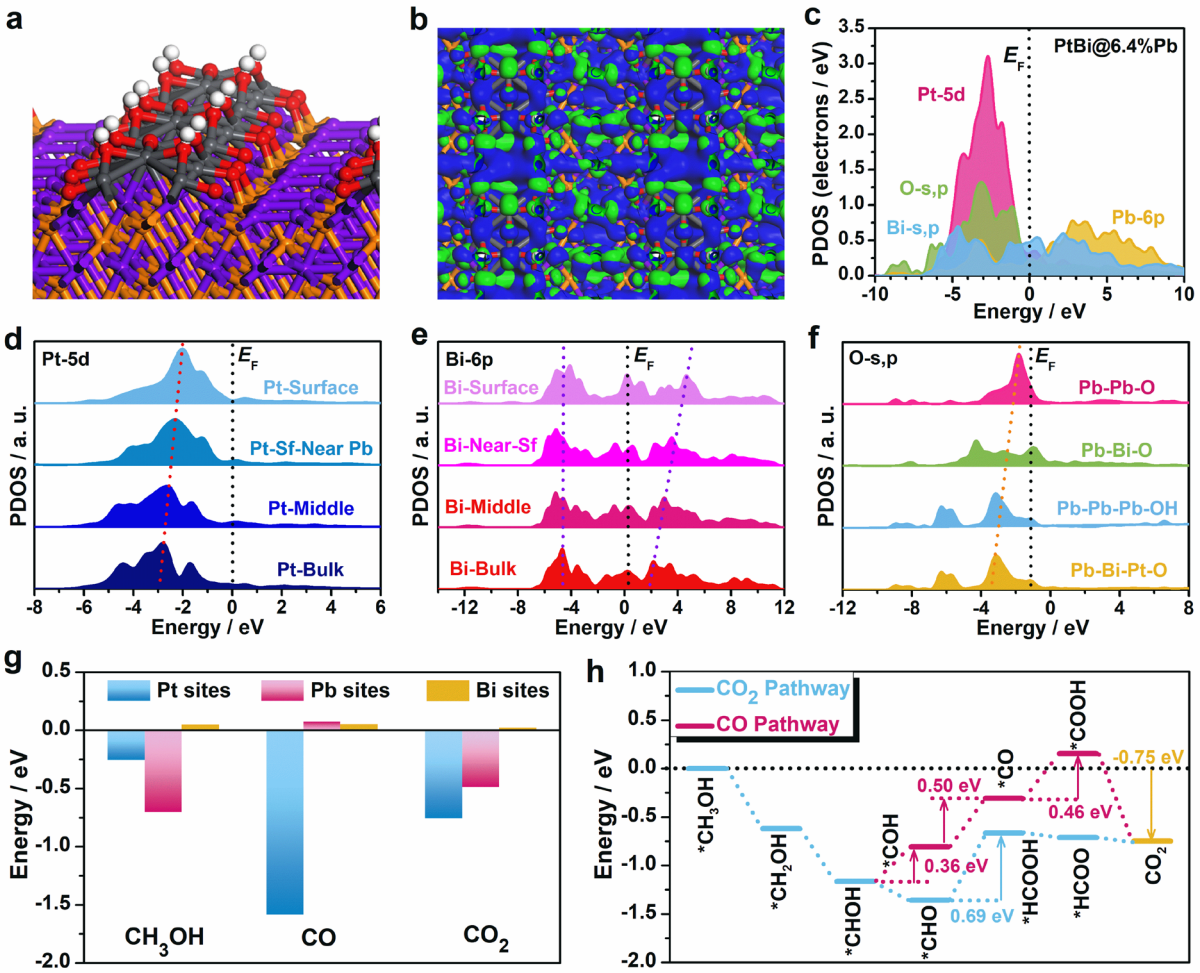

Figure 4. a) The lattice structure of PtBi@6.4%Pb from the side view. Purple, Orange, Grey, Red, and White spheres represent Pt, Bi, Pb, O, and H atoms, respectively. b) 3D contour plot of electronic distributions of PtBi@6.4%Pb from the top view. The blue isosurface = bonding orbitals and the green isosurface = anti-bonding orbitals. c) PDOS of PtBi@6.4%Pb. Site-dependent PDOS of (d) Pt-5d, (e) Bi-6p, and (f) O-s, p in PtBi@6.4%Pb. g) The adsorption comparison of CH_3OH, CO, and CO_2 on different Pt, Pb, and Bi sites in PtBi@6.4%Pb. h) The energetic trend of the MOR pathway.

TOC

Hexagonal PtBi intermetallic nanoplates inlaid with sub-monolayer Pb oxyhydroxide are constructed and resolved at the atomic level. Originating from the isolation and surface modification of Pt atoms via Bi/Pb species, the well-defined PtBi@6.4%Pb nanoplates exhibit significantly enhanced activity, durability, and anti-CO poisoning towards the methanol electro-oxidation in alkaline electrolyte, and the notable effects of Pb oxyhydroxide patching are revealed by DFT calculations.

Keyword: intermetallic; Pb oxyhydroxide; methanol oxidation; electrocatalysis.

Wen Chen#, Shuiping Luo#, Mingzi Sun, Min Tang, Xiaokun Fan, Yu Cheng, Xiaoyu Wu, Yujia Liao, Bolong Huang and Zewei Quan**

Hexagonal PtBi Intermetallic Inlaid with Sub-Monolayer Pb Oxyhydroxide Boosts Methanol Oxidation